Title

Surface Lattice Plasmon Resonances by Direct In Situ Substrate Growth of Gold Nanoparticles in Ordered Arrays.

Journal

Advanced Materials, 34(37)

Authors

Vinnacombe-Willson, Gail
Conti, Ylli
Jonas, Steven
et al.

Publication Date

2022-09-01

DOI

10.1002/adma.202205330

Peer reviewed

HHS Public Access

Author manuscript

Adv Mater. Author manuscript; available in PMC 2023 September 01.

Published in final edited form as:

Adv Mater. 2022 September ; 34(37): e2205330. doi:10.1002/adma.202205330.

Surface lattice plasmon resonances by direct *in situ* substrate growth of gold nanoparticles in ordered arrays

Gail A. Vinnacombe-Willson,
Department of Chemistry and Biochemistry, University of California, Los Angeles, Los Angeles, California 90095, United States

Ylli Conti,
Institute of Materials Science of Barcelona, ICMAB-CSIC, Campus UAB, 08193 Bellaterra, Spain

Steven J. Jonas,
California NanoSystems Institute, University of California, Los Angeles, Los Angeles, California 90095, United States; Department of Pediatrics, David Geffen School of Medicine, University of California, Los Angeles, Los Angeles, California 90095, United States

Paul S. Weiss,
Department of Chemistry and Biochemistry, University of California, Los Angeles, Los Angeles, California 90095, United States; Department of Bioengineering, University of California, Los Angeles, Los Angeles, California 90095, United States; Department of Materials Science and Engineering, University of California, Los Angeles, Los Angeles, California 90095, United States; California NanoSystems Institute, University of California, Los Angeles, Los Angeles, California 90095, United States

Agustín Mihi,
Institute of Materials Science of Barcelona, ICMAB-CSIC, Campus UAB, 08193 Bellaterra, Spain

Leonardo Scarabelli
Institute of Materials Science of Barcelona, ICMAB-CSIC, Campus UAB, 08193 Bellaterra, Spain

Abstract

Precise arrangements of plasmonic nanoparticles on substrates are important for designing optoelectronics, sensors, and metamaterials with rational electronic, optical, and magnetic properties. Bottom-up synthesis offers unmatched control over morphology and optical response of individual plasmonic building blocks. Usually, the incorporation of nanoparticles made by bottom-up wet chemistry starts from batch synthesis of colloids, which requires time-

lscarabelli@icmab.es .

Author Contributions

Experiments were designed by GAVW and LS. Data were collected by GAVW, LS, and YC. GAVW and LS led the optimization of the HPC stencil fabrication. GAVW, LS, and YC performed the synthesis optimization of the AuNPs into arrays. Morphological characterization of the AuNPs was performed by GAVW and LS. Optical characterization was carried out by LS and YC. The manuscript was written by GAVW, LS, SJJ, PSW, and AM, with assistance from all other authors. All authors have given approval to the final version of the manuscript.

Supporting Information

Materials and detailed experimental procedures for the fabrication of HPC stencils and *in situ* gold nanoparticle growth. Parameters for SEM and optical characterization of the nanoparticle arrays. Additional characterization of the array yield and observed products.

consuming and hard-to-scale steps like ligand exchange and self-assembly. Herein, we develop an unconventional bottom-up wet-chemical synthetic approach for producing gold nanoparticle ordered arrays. Water-processable hydroxypropyl cellulose stencils facilitate the patterning of a reductant chemical ink on which nanoparticle growth selectively occurs. Arrays exhibiting lattice plasmon resonances in the visible region and near infrared (quality factors >20) were produced following a rapid synthetic step (<10 min), all without cleanroom fabrication, specialized equipment, or self-assembly, constituting a major step forward establishing *in situ* growth approaches. We further demonstrate the technical capabilities of this method through modulation of the particle size, shape, and array spacings directly on the substrate. Ultimately, establishing a fundamental understanding of *in situ* growth has the potential to inform the fabrication of plasmonic materials, opening the door for *in situ* growth fabrication of waveguides, lasing platforms, and plasmonic sensors.

Graphical Abstract

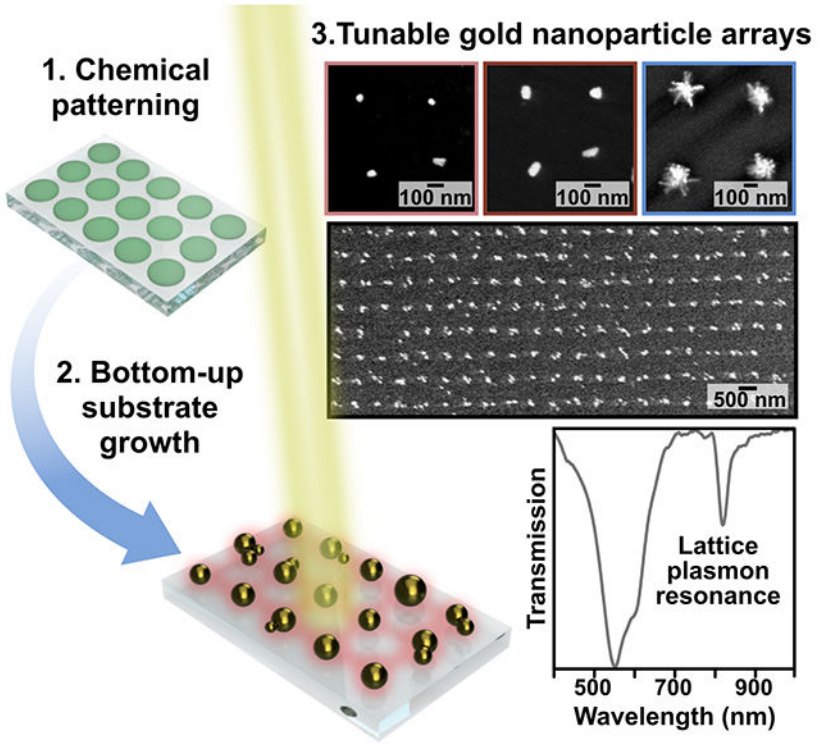

Gold nanoparticle plasmonic ordered arrays were fabricated by an unconventional *in situ* approach where gold precursors are reduced directly at specific pre-patterned locations on substrates. Nanoparticle morphology and array periodicity are easily tuned using this method. The substrates exhibit far-field plasmonic coupling *via* the emergence of lattice plasmon resonances, constituting a major step forward for *in situ* growth techniques.

Keywords

plasmonic arrays; *in situ* growth; bottom-up synthesis; lattice plasmon resonance

1. Introduction

For plasmonic nanoparticles, the resonant condition of collectively oscillating conduction electrons occurs at specific frequencies of light depending on the nanoparticle size, shape, material, and local dielectric environment.[1] This localized surface plasmon resonance (LSPR) effect can confine light in subwavelength volumes,[2] resulting in the generation of an enhanced electric field. However, these resonances are typically short lived, due to intrinsic high radiative optical losses that limit the associated quality factors (<10).[3] Nonetheless, arranging plasmonic nanoparticles into ordered arrays emerged as a convenient strategy to overcome this limitation and to boost the quality factors of the system. In this configuration the optical losses associated with LSPRs can be compensated under Bragg conditions by hybridization with the scattered waves in the plane of the array close to the position of the Rayleigh-Wood anomalies.[3] This compensation generates lattice plasmon resonances, and offers an additional possibility for tuning the optical properties, depending on the angle of illumination and the geometrical parameters of the array.[3] Due to their narrow bandwidth (<2 nm) and long lifetimes,[3–5] lattice plasmon resonances already impact the enhancement and manipulation of light-matter interactions,[6–8] sensing,[9–12] displays,[13] information storage,[14] and anti-reflective materials.[15]

The development of a simple, scalable, and rapid technique that combines the benefits of top-down and bottom-up methods would improve access to finely tuned plasmonic ordered arrays tailored to desired applications.[16–18] As of now, top-down methods benefit from their control over the positions of the particles and the generalizability of the substrates, [5,6,19] where bottom-up approaches offer control over the surface chemistry and particle size and shape.[1,16,18–20] Capillary-assisted, electrophoretic, and templated self-assembly can be used to generate nanoparticle arrays from colloidal building blocks, offering affordable alternatives to top-down electron beam lithography, focused ion beam lithography, and electro- and thermal deposition.[18,20,21] Despite these advantages, beginning from colloidal suspensions often involves multistep, time-consuming processes that limit scalability. For instance, liters-scale batch pre-synthesis requires precise temperature and additional rate control and ligand exchange requires the addition of large excesses of capping ligands and multiple centrifugation steps.[18,22–24] Furthermore, the requirement of clean-room facilities, costly specialized equipment, and complex self-assembly steps present barriers preventing accessibility of plasmonic substrates.[25–27]

In situ growth is an unconventional approach where plasmonic structures are formed starting from inorganic precursors directly on the target substrate material without any initial colloidal synthesis steps.[28–32] The particles nucleate on the substrate, therefore, this process does not involve any batch synthesis, self-assembly, or ligand exchange, and time-consuming procedures can be circumvented. So far, the possibility to direct growth into tunable nanometric patterns has proven difficult to achieve *via in situ* growth. [31–35] Recent strategies for site-directed *in situ* gold nanoparticle growth include crack-templated reduction lithography and similar methods.[32,35] Despite the possibility of creating single-nanoparticle-wide features using these techniques, the patterns accessible are limited to lines with resolutions of microns to hundreds of nanometers. Chemical patterning *via* microcontact printing has been combined with *in situ* growth to grow gold

nanoparticles selectively on tunable micron-scale features, but with limited control over the nanoparticle morphology.[33] Similar results were observed with *in situ* growth on top-down lithographically patterned chemical layers.[34] Block-copolymer micelle lithography represents a leading technique applying *in situ* growth, where addressable structures comprised of shape- and size-controlled plasmonic units are uniformly and reproducibly created with single-particle resolution.[36–38] However, standard block-copolymer micelle lithography is generally limited to array periodicities up to ~300 nm, preventing access to lattice plasmon resonances in the visible and infrared.[36–39] Moreover, due to the reliance of the patterning on the assembly of block copolymer micelles, the arrays are typically constrained to hexagonal lattices and the casting process can take up to a few weeks (unless combined with additional top-down or soft-lithographic steps).[36–38] Current limitations of *in situ* growth methods include: (*i*) controlling the particle morphology/uniformity, (*ii*) fabricating easily modifiable patterns (and with good selectivity), and (*iii*) producing arrays with sufficient quality to sustain lattice plasmon resonances. Ultimately, these barriers have reduced the popularity of *in situ* growth methods for the fabrication of plasmonic substrates compared to top-down nanofabrication (such as electron beam lithography) and/or the implementation of colloidally prepared nanoparticles. Furthermore, comprehensive mechanistic understanding of gold nanoparticle formation on substrates requires further study, and relatively little work has addressed fundamental synthetic aspects of *in situ* growth, especially compared to the body of work that has been developed for colloidal synthesis.

Here, we establish and demonstrate a straightforward *in situ* growth approach targeting tunable plasmonic lattices following rapid bottom-up growth of gold nanoparticles onto chemically patterned reactive areas created by soft lithography. To fabricate these structures, water-soluble hydroxypropyl cellulose (HPC) sacrificial hole masks (or stencils), were applied to create patterned regions containing gold nanoparticle growth-active chemical ink. Subsequent site-selective growth of gold nanoparticles was performed with the addition of a droplet of growth solution onto the chemically patterned substrates in one rapid (<10 min), single synthetic step. We demonstrate that the composition of the growth solution can be modulated to alter the size and shape of the particles as they grow on the substrate. We apply one-step direct surface growth to generate lattice plasmon resonances, showing that *in situ* growth techniques can be used for engineering plasmonic materials with low optical losses. The benefits of plasmonic nanoparticle patterning and direct engineering of lattice plasmon resonances by *in situ* growth can contribute to the development of more efficient quantitative chemical and biological sensors,[9–12] plasmonic catalytic substrates,[40–42] and biomedical platforms,[43–46] offering far-reaching impacts in a broad range of fields.

2. Results and Discussion

2.1. Chemical Nanopatterning with Thermal Nanoimprint Lithography

Gold nanoparticle arrays were fabricated on polydimethylsiloxane (PDMS) substrates following the creation of nanometric chemical patterns following a scalable and versatile soft lithographic method. Specifically, water-processable HPC stencils were prepared *via* thermal nanoimprint lithography (t-NIL) as shown in Figure 1A and applied to direct gold

nanoparticle growth to specific areas containing a strong chemical reductant.[47–50] Briefly, in the t-NIL process, aqueous solutions of HPC were spin-coated onto the substrate, then the film was placed in contact with a hard PDMS (hPDMS) mold. Pressure was applied to the mold as the substrate was heated above the HPC glass transition temperature (140 °C), generating patterned holes shaped by the mold (optimization of the applied pressure and substrate treatments are shown in Figure S2). We demonstrate high-fidelity patterning of films ranging in height from tens to a few hundred nm (~30-330 nm), by comparing the measured and simulated differential refraction spectra for HPC thin films prepared with identical procedures on silicon (Figures 1B and S3, experimental details in the Supporting Information). After t-NIL, the imprinted photonic structures confer iridescence to the patterned films, as shown in Figures 1C and S3. Successful array transfer was confirmed *via* scanning electron microscopy (SEM) in films as low as ~30 nm (Figure 1D–F).

This result seems counterintuitive, because normally with t-NIL, uniform patterns are not attainable with HPC volumes that do not match the negative volume of the stamp, which in our case corresponds to a >250 nm film height (Scheme S6, Table S1, and calculations in the Supporting Information). Electron microscopy analysis shows that the PDMS substrate is imprinted following the t-NIL process (Figure 1G,H). Therefore, we hypothesize that the key to patterning films nearly an order of magnitude lower in height than the normally required minimum is the implementation of the deformable receiving substrate, which helps to push the HPC into the vacant features as shown in Figure 1I.[25–27,51] This feature has important implications for the thickness of the residual layer. In standard t-NIL on rigid substrates, residual material remains in the imprinted features, usually measuring *ca.* 20 nm in height for the patterns used here.[49,50] The removal of the excess material necessitates anisotropic reactive ion etching and cleanroom processing. Since we can pattern significantly thinner films, we estimate that the residual layer is accordingly greatly reduced (Figure S4,5). Consequently, a quick (30 s) isotropic UV-ozone etch can effectively remove the excess HPC remaining in the holes. This etching step was successful for all HPC formulations that gave films with lower volume than the negative volume of the stamp (Figure S6). Overall, the described procedure enables the reliable fabrication of HPC stencils with nanometric hole features (lattice parameter, Λ = 600 nm) without the use of any specialized or costly equipment or cleanroom fabrication. In addition, the same modified t-NIL technique can be extended from free-standing PDMS to glass-supported PDMS, improving the ease of sample handling (Scheme S2, Figure S7, Materials and Methods).

In the next step, the HPC stencils were used for the *in situ* growth of gold nanoparticles into ordered plasmonic arrays as shown in Figure 2A: following the 30 s UV-ozone etch, the polymethylhydrosiloxane chemical ink was applied on top of the stencil (Figure 2A). The integrity of the pattern of the HPC film is retained after the UV-ozone treatment and ink application steps as confirmed by SEM (Figure S4). Then, the HPC stencil was dissolved in water, and the chemically patterned substrate was dried with an air gun. Finally, a fixed volume (150 μL) of gold nanoparticle growth solution containing surfactant cetyltrimethylammonium chloride or bromide as capping ligands, ascorbic acid as a mild reducing agent, and the gold inorganic precursor tetrachloroauric acid, $HAuCl_4$, was spread on the surface and was allowed to react for 10 min with the physisorbed ink (see Supporting Information section “In situ gold nanoparticle growth,” Scheme S4 for more details on

the procedure and detailed composition of the solution). Following optimization, patterned particle growth into patterned arrays (~0.5 mm^2 area) was confirmed by SEM (Figure 2B). The grown particles are mechanically stable and remain on the substrate after thorough rinsing and drying steps.

Decreasing the competition between nuclei formation on the substrate and nucleation in the growth solution is critical for successful *in situ* growth into patterns and for fundamental *in situ* size- and shape-control.[29,30,52–55] In standard colloidal gold nanoparticle seed-mediated synthesis, the nucleation and growth steps are spatiotemporally separated to control the final particle morphology.[1,56] First, small gold nuclei (also known as seeds) are uniformly grown and later added to a separate solution where they grow in a controlled manner into desired sizes and geometries. The nucleation step normally incorporates a strong reductant such as sodium borohydride for the fast, uniform formation of seeds from the gold precursor. The following growth step instead includes weaker reductants, such as ascorbic acid, capable of reducing Au^{III} to Au^{I}, but confining the final reduction to Au^{0} to the seed surface, promoting controlled growth. The seed-mediated synthesis scheme ensures suppression of later secondary nucleation events from occurring in the growth solution that would negatively affect size distribution and shape yield.[1,57]

One of the most important aspects explored here is the limitation and control of secondary nucleation, which has proven to be a particularly difficult challenge for *in situ* growth systems.[46,53,54,58] Here, the strong reductant ink is applied only on the substrate to mimic the spatially selective nucleation and growth processes used in colloidal synthesis, while the mild reductant ascorbic acid is added to the growth medium to facilitate the first reduction step of the gold salt from Au^{III} to Au^{I}. Although in our *in situ* growth scheme, we are only providing strong reductants on the surface of the substrate, colloidal nanoparticles can still spontaneously form from the precursors in the growth solution. Thus, secondary nucleation for *in situ* systems can be described as the uncontrolled formation of nuclei away from sites explicitly containing the strong reductant, which contributes to irreproducible consumption of reagents and solution-deposited particles outside the pattern (Figure 2C).

Even though nucleation can be achieved with the sole use of the physisorbed ink, our motivation behind adding ascorbic acid is to reduce the growth time and use of lower concentrations of gold precursor.[30,59,60] In fact, using only a surface-bound strong reductant usually requires ~5 times more gold salt and hours- to days-long incubation.[31,32,35] Continuing with the goal of limiting secondary nucleation, we identified factors that could lead to the undesired spontaneous formation of colloids: (i) the presence of impurities in the growth solution, (ii) growth rate, and (iii) excess ink leeching into solution. Regarding impurities, the water source is known to play important roles in colloidal synthesis, especially for the synthesis of anisotropic particles.[61,62] Recent work shows that faster growth kinetics can favor colloidal nucleation over nucleation on the substrate.[54] Therefore, we modulated the rate of the reaction by changing the type and concentration of the surfactant (cetyltrimethylammonium chloride or bromide, CTAC or CTAB, respectively). Lastly, we tested different inking methods and ink concentrations. The appearance of LSPR peaks evaluated by ultraviolet-visible spectroscopy indicated the occurrence of secondary nucleation, and the maximum intensity of the peaks was monitored

over 15 min to track the severity of unwanted nuclei formation under different growth conditions (Figure 2D,E; Figure S8). Overall, growth solutions containing high-performance liquid chromatography (HPLC) grade water, and 25-50 mM CTAB gave the least secondary nucleation (Figure 2D). This optimized growth formulation was fixed and the application of chemical ink *via* different routes was tested. Aside from vapor deposition, the least amount of secondary nucleation was observed when dilute (1% or 0.1%) solutions of the ink were spin-coated onto the substrate (Figure 2E). Spin coating dependably produced patterns, and all conditions appeared to give similar nucleation site densities (Figures S4, S9, S10). Therefore, the 0.1% solution was selected for the following sections. After 10 min of growth, the products appeared to have different crystal structure and twinning, and isotropic products, triangles, rods, and other platelets could be observed (Figure 2F–I). In the next section, we explore size and shape-modification of the products.

2.2 *In Situ* Size and Shape Modification

Although little prior work has addressed mechanistic aspects of substrate-grown particles,[53–55,63–66] fundamentals of *in situ* growth remain vastly unexplored compared to colloidal batch systems.[59] Limiting the growth-active areas to diameters < 100 nm has the potential to enable tighter control over both nucleation and growth conditions. Next, we demonstrate the capability to modulate the size and morphology of the synthesized particles by changing the growth medium constituents and parameters, following concepts derived from colloidal synthesis.

Nanoparticle size was controlled by tuning the growth times between 1 min and 10 min using the optimized growth solution from Figure 2 containing cetyltrimethyammonium bromide as a capping ligand and ascorbic acid as the mild reductant (Figure 3A–D, see Materials and Methods section for details). After 1 min of growth, the average particle size reaches 40 ± 14 nm (Figure 3E), which is relatively fast compared to colloidal synthesis.[24,67,68] At 2 min, the products nearly double in size to 70 ± 30 nm (Figure 3F). Growth times of 5 and 10 min result in nanoparticles with similar diameters (120 ± 40 nm and 110 ± 40 nm, respectively, Figure 3G,H). This behavior is consistent with other *in situ* growth studies.[28,58,69,70] Another interesting aspect to consider is the shape distributions of the nanoparticles grown. In colloidal synthesis of gold nanospheres, mixtures of various anisotropic (elongated structures, platelets) and isotropic (multi-twinned objects, cubes, pyramids) products are obtained if no shape-control strategy is used during growth.[71–73] We observe similar behavior in the case of *in situ* grown particles. Even though the limitations of environmental scanning electron microscopy prevent us from distinguishing between different isotropic products (Figure 2F), we were able to identify platelets (Figure 2G,I) and rod-shaped geometries (Figure 2H), enabling us to evaluate their percentages and/or shape yield. Along with a change in the average nanoparticle diameter, shorter growth times were associated with lower percentages of total platelet and rod-shaped products. We estimate that the percentage of isotropic products decreased from ~60% at 10 min to ~90% at 1 min (n=150 nanoparticles, Figure S11, Table S2). After 5 min, the nanoparticles formed at the specified nucleation sites no longer increase in size, possibly due to the onset of secondary nucleation effects. This hypothesis is supported by our evaluation of the

patterning yield presented in Table S3, where the percentage of particles outside the pattern slightly increases from 10% to 14% between 5 and 10 min.

Regarding patterning evaluation, various kinds of defects in the arrays are observed (Figure 3I–J). Standard defects include vacancies (*purple circles*), multiple particles per region (*pink circles*), and particles outside the patterned region (*green arrows*). The patterning yield was evaluated as the percentage of ink-containing regions that produced nanoparticles across all growth times as ~80% (detailed evaluation summarized in Figure S12, Table S3). The total percentage of nanoparticles located within the growth active regions was estimated to be ~90%, indicating a strong preference for nucleation and growth within the pattern features due to the chemical contrast created by the presence and absence of the ink.

The identification of the sources of defects could assist in future development of our *in situ* growth method; therefore, we next elaborate on this topic. Nanoparticles outside of the pattern (~10% of all particles) result either from secondary homogeneous nucleation events in the growth solution (followed by particle deposition on the surface), non-specific spontaneous nucleation on regions without ink, or defects in the HPC mask. The appearance of vacancies in the electron microscopy images could be caused by resolution limitations of environmental scanning electron microscopy, which complicates imaging particles smaller than 2 nm. If instrument resolution was the primary cause of observed vacancies, one would expect these small nuclei to grow eventually into larger, more easily measurable nanoparticles. However, the percentage of vacancies remains *constant* when growth time is increased from 1 to 10 min; therefore, we infer that the vacancies do not contain nanoparticles. Another hypothesis to explain the vacancies can be related to defects in the HPC stencil, causing local removal of the ink during the washing step. The exploration of different chemical inks to increase the chemical contrast of the patterned regions and the substrate could be pursued in the future to reduce the abovementioned defects. Finally, both the presence of nanoparticles that are not centered in the patterned area and the growth of multiple particles in certain regions can arise from the size mismatch between the growing particles and the patterned features, with the latter being much larger (>270 nm). Nonetheless, the average number of nanoparticles per patterned area corresponds to 2 particles per circular region (not counting vacancies). This is an important observation because it suggests that once the initial nuclei are formed, their growth is favored over the later formation of new nuclei. The formation of new nuclei is disfavored due to the preference for continued growth on the already-formed nuclei and/or due to charge screening affecting the transport of gold salt to the substrate.[61,71] Moreover, this statistic gives us an estimate of the number of particles on each substrate as approximately ~2×10^8 particles/substrate, or ~2×10^9 particles/mL of growth solution (assuming 100% yield of the t-NIL and ink patterning). The seed concentration in colloidal synthesis is usually 2-4 orders of magnitude higher (typical values for colloidal synthesis range between 10^{11} and 10^{13} seeds/mL of growth solution), giving us a much higher $HAuCl_4$ to nanoparticle ratio.[61,68] This difference provides an explanation for the speed of growth and offers possible improvements to target smaller nanoparticles and/or slower kinetics.

Next, we demonstrate generating anisotropic shapes directly on the substrate through post-modification and overgrowth of the arrays prepared after 5 min growth. Previously, *in situ*

overgrowth has been performed on colloidal assemblies to create unique geometries, such as Janus nanostructures, core-shell, hybrid, and anisotropic/branched structures,[74,75] which enable control over the plasmonic near-field with applications for photothermal or sensing applications, for example.[12,46,76,77] Here, we target overgrowth of branched nanostars, which are attractive due to high localization of electromagnetic fields present at their sharp tips,[46,76,78] their high extinction in the near-infrared biological window, and their capability for thermoplasmonic heating.[46,79] The nanoparticle arrays were overgrown by subsequent incubation in a nanostar growth solution containing additional gold precursor and shape-directing reagents (silver nitrate, laurylsulfobetaine, hydrochloric acid, and ascorbic acid, Figure 4A). Similar to the first growth step, synthetic conditions were optimized to minimize secondary nucleation away from the substrate within the 5 min overgrowth time by lowering the pH of the growth medium, which limits the reducing strength of ascorbic acid.[46] Following the overgrowth step, the substrate exhibited a change in color from red to dark blue. The extinction spectra after 5 min of standard nanoparticle growth with the cetyltrimethylammonium bromide growth solution gives one dominant LSPR dip at 575 nm, and the samples following 5 min of nanostar overgrowth exhibit high extinction in the near infrared region at 985 nm, matching the expected plasmonic response Figure 4B.[46] The corresponding colloid recipe for the one used here generally results in three main products: spheres, and low and high aspect ratio nanostars.[46,76] However, electron microscopy characterization interestingly showed a high yield of one major, highly branched product (Figure 4C,D). The yield of the nanostar arrays over a larger area (measuring *ca.* 2000 μm^2) can be appreciated in Figure 4E. Altogether, the data presented in Figure 4 indicate that although certain concepts might transfer from colloidal to substrate growth (*e.g.*, applying shape-directing reagents to promote anisotropic growth), important differences remain between the two environments that can significantly affect the shapes of the final products. The *in situ* surface growth strategy reported here represents an ideal platform for the exploration of such effects.[46]

2.3 Geometrical Tuning of the Array and Lattice Plasmon Resonance Characterization

Perhaps the most striking advantage of combining t-NIL and *in situ* growth resides in the preparation of ordered plasmonic arrays with arbitrary geometries, achieving control at the same time over both LSPRs and lattice plasmon resonances.[47–50] Although past and recent work proposed this possibility in relation to other *in situ* growth schemes, lattice plasmon resonances have not previously been demonstrated experimentally using only direct surface growth.[36–39] The spatial and geometrical constraints of the state-of-the-art methods prevent engineering lattice plasmon resonances (as well as more complex light-matter interactions),[80–82] limiting the application of *in situ* growth for the design of metasurfaces and intricate plasmonic systems. Our *in situ* growth approach overcomes two major barriers, namely the requirement for lengthy self-assembly steps and the flexibility in array periodicity by modifying the hPDMS stamp.[50] Here, we measure lattice plasmon resonances for arrays with lattice parameters (Λ) of 400 and 500 nm, in addition to the Λ=600 nm samples shown in Figures 1, 3 (Figures 5A–F, S13–S15). Patterned *in situ* growth was achieved in all cases.

With the intention of maximizing the generation of lattice resonances through far-field coupling between the plasmonic units of the array, the particles were covered with a thin

layer of soft PDMS after growth was complete. This step ensures a uniform refractive index environment around the plasmonic lattices, facilitating the propagation of the scattered field within the lattice plane.[3] Sharp lattice plasmon resonances were observed in the transmission profile under this refractive index matching condition (sample preparation details are given in the Supporting Information and Scheme S5, Figure 5G–J) giving, to the best of our knowledge, the first demonstration of lattice plasmon resonances *via* a purely *in situ* synthetic route, all without batch synthesis, self-assembly, top-down fabrication, nor costly and specialized equipment. Overall, this result shows that *in situ* growth can offer an inexpensive, simple, and rapid alternative for accessing collective plasmonic responses.

As expected, the wavelengths of the lattice plasmon resonances depend on the lattice parameter used for the preparation of the HPC masks (Figure 5G). Specifically, the most intense lattice plasmon resonances are expected to emerge in proximity to the first-order diffraction line, the spectral position of which can be predicted using the following simplified equation:[17]

$$\lambda = \Lambda_{x,\,y}\,(n \pm sin\theta) \tag{1}$$

where $\Lambda_{x,\,y}$ represents the lattice parameters in the two orthogonal in plane directions, n is the refractive index of the surrounding medium, and θ is the illumination incidence angle. At normal incidence, where θ is defined as zero, for a square lattice where $x = y$, and with n_{PDMS} estimated to be 1.4, the predicted wavelengths can be calculated as: 560 nm for Λ = 400 nm, 700 nm for Λ = 500 nm, and 840 nm for Λ = 600 nm. In the 400 nm lattice parameter samples, the predicted lattice plasmon resonance overlaps with the LSPR of the gold nanoparticles and can be identified as a shoulder at 560 nm in the transmission spectrum. For the 500 nm lattice, a dip is observed at 698 nm, close to the predicted lattice plasmon resonance position. In the 600 nm lattice sample, the lattice plasmon resonance is observed at 826 nm (Figure 5G). The discrepancies compared to the predicted positions are common and can be attributed to factors including the effects of the CTAB gold nanoparticle coating, and/or the differences in PDMS refractive index as a function of composition and curing conditions.[21]

The identification of the aforementioned dips as lattice resonances is confirmed by measuring their spectral variation with illumination incidence angle (Figure 5H–J).[22] The dashed lines in Figure 5H–J are analytical calculations of the angular dependence of the Rayleigh-Wood anomalies. Apart from refractive index and lattice parameter, this dependence will also be modulated by the azimuthal angle of the array relative to the illumination (see discussion in Materials and Methods). Additionally, the quality of the Λ = 600 nm array is also confirmed by the appearance of a second-order diffraction line (Figure 5J). Overall, the experimental data matched the predicted behavior, confirming the presence of lattice resonances.

Additionally, the quality of the observed lattice plasmon resonances was evaluated by calculating the quality factor (Q_F):

$$Q_F = \frac{\omega}{\Delta(\omega)} \quad (2)$$

where ω is the spectral peak position, and Δ(ω) is the full width at half maximum of the peak. Using this relationship, we evaluate Q_F = 29 for Λ = 600 nm and Q_F = 21 for Λ = 500 nm. For the Λ = 400 nm array, we are unable to estimate the Q_F since the diffraction line is blue-shifted relative to the lattice resonance peak, producing an asymmetric Fano profile, as described in a prior publication[22] (details on Q_F calculations are in the optical characterization section of the Supporting Information).

The Q_F for single-nanoparticle arrays prepared from colloidal suspensions typically fall within the range of Q = 10-30,[3,22,83] Thus, the performance of our arrays are on par with state-of-the-art methods based on single-particle assembly, despite the patterning defects and deviations in nanoparticle morphology that we observe. These results may be unexpected considering that our patterning yield is ~80% (Figures 3IJ and S12, Table S3) and our shape-yield is ~80-90% (Figure S11 and Table S2), and any array defects would lead to broadening of the lattice resonance.[3,22,84] However, recent simulations by Manjavacas and co-workers suggest that by reducing the dimensions of the repeating unit below 100 nm, it is possible to achieve narrow LPRs, and that this effect is even more dramatic for realistic finite systems.[84] These observations lead us to hypothesize that the reduced dimensions of our *in situ* grown nanoparticles, and the absence of optical losses due to strong near-field coupling within the repeating unit (as for cluster plasmonic arrays), explain our observation of relatively sharp lattice resonances despite the presence of defects. Even though the fabricated arrays are less uniform than those prepared by state-of-the-art top-down[3,85] or colloidal synthesis/self-assembly approaches,[22,23] the demonstration of lattice plasmon resonances with bottom-up *in situ* substrate growth highlight its potential as a straightforward and easily accessible route for plasmonic materials engineering.

3. Conclusions and Prospects

A modified t-NIL protocol was used to pattern HPC thin films on soft polymeric substrates. This technique produced periodic structures with minimal residual layers such that water-processable sacrificial stencils can be created in a standard laboratory environment without special equipment. The sacrificial HPC masks were used for chemical patterning and subsequent site-selective bottom-up gold nanoparticle growth. The particle size and shape were controlled directly on the substrate by altering the growth time and growth media composition, respectively. The use of t-NIL provides improved flexibility for modifying the pattern increments over a wide range by changing the mask features without adjusting the patterning process or increasing the processing time. Following optimization of the chemical inking method and the nanoparticle growth solution, lattice plasmon resonances were demonstrated for arrays with periodicities of 400, 500, and 600 nm, giving tunable lattice plasmon resonances from the visible to the near infrared. The versatility in tuning the array geometry can be applied for potentially targeting lattice geometries giving collective responses beyond the near infrared, into the mid- or even far-infrared regions. The developed method overcomes limitations that have, until now, prevented the realization

of lattice plasmon resonances using solely *in situ* growth, constituting significant progress for this class of approaches. Future work can target the fabrication of hybrid materials and superstructures with multiple synthetic steps, in order to engineer complex optical responses, like what has been achieved *via* metal nanoparticle-polymer systems.[86,87] The design and fabrication of sensors relying on surface-enhanced Raman spectroscopy can also be the target of future exploration,[29,30,65] especially since patterning can assist in controlling hot-spot density.[88]

Regarding fundamental synthetic aspects, understanding the roles of substrate wettability, particle-substrate interaction, secondary nucleation, the balance of reducing agents on the substrate and in solution, effects of surface charge, chemical environment, and screening effects can help to create more reliable protocols achieving gold nanoparticle arrays and pave the way for new synthetic possibilities in the future.[39,89–91] Shape control for *in situ*-grown particles has only been briefly studied compared to colloidally synthesized particles and the need to probe various aspects of the growth thoroughly remains. In this regard, the *in situ* growth method presented here is versatile for future investigations studying wet-chemical shape control and selective surface growth. Furthermore, because the nanoparticles are fixed on the substrate, colloidal stability no longer represents a barrier to be considered, providing greater opportunities for testing unconventional growth conditions (*e.g.*, surfactantless synthesis) or facile tailoring of the nanoparticle ligands. We anticipate that nanoparticle-substrate interactions will represent important aspects to explore, which can potentially be tuned *via* the selected metal,[92,93] selected ink, or the chosen substrate. The chosen substrate represents even more opportunities, *i.e.*, replacement of PDMS with different soft polymers,[94,95] conductive polymers,[96,97] hydrogels[98] and two-dimensional materials.[99,100] In addition, the physical or chemical properties of the substrate could potentially be used as templates to faciliate the rotaional order of products.[101,102] Ultimately, the presented methodology can bring a new perspective for the development of innovative synthetic paradigms for the growth of plasmonic nanoparticles and can impact the fabrication of solid-state platforms that take full advantage of the catalytic, optical, and magnetic properties of plasmonic nanoparticles.

Supplementary Material

Refer to Web version on PubMed Central for supplementary material.

Acknowledgments

We thank Dr. Camilla Dore for her advice and contributed expertise on the fabrication of HPC films. The authors extend their gratitude to Jose Mendoza Carreño for his assistance with the optical characterization of the gold nanoparticle arrays. This project had received funding from the Spanish Ministry of Science and Innovation through grants FUNFUTURE (CEX2019-000917-S), (FUNFUTURE, in the framework of the Spanish Severo Ochoa Centre of Excellence program) and PID2019-106860GB-I00 (HIGHN). LS and AM thank the Spanish National Research Council (CSIC) for funding via the I-LINK 2020 international travel grant, which facilitated international exchange period necessary for completion of this work. LS and YC research is supported by the 2020 Post-doctoral Junior Leader-Incoming Fellowship by “la Caixa” Foundation (ID 100010434, fellow-ship code LCF/BQ/PI20/11760028). YC acknowledges financial support from the UAB under the auspices of the UAB material science doctoral program. GAVW thanks the UCLA graduate division for funding through the University of California Office of the President Dissertation Year Fellowship. SJJ acknowledges support from the National Institutes of Health (NIH) Common Fund through a NIH Director’s Early Independence Award co-funded by the National Institute of Dental and Craniofacial Research and Office of the Director, NIH Grant

DP5OD028181. SJJ and GAVW acknowledge support through a Scholar Award from the Hyundai Hope on Wheels Foundation for Pediatric Cancer Research. PSW thanks the National Science Foundation for support through Grant #CHE-2004238.

References

[1]. Liz-Marzán L, Colloidal Synthesis of Plasmonic Nanometals, CRC Press, 2020.

[2]. Willets KA, Van Duyne RP, Annu. Rev. Phys. Chem 2007, 58, 267. [PubMed: 17067281]

[3]. Kravets VG, Kabashin AV, Barnes WL, Grigorenko AN, Chem. Rev 2018, 118, 5912. [PubMed: 29863344]

[4]. Adato R, Yanik AA, Wu C-H, Shvets G, Altug H, Opt. Express 2010, 18, 4526. [PubMed: 20389465]

[5]. Wang D, Yang A, Hryn AJ, Schatz GC, Odom TW, ACS Photonics 2015, 2, 1789.

[6]. Zhou W, Dridi M, Suh JY, Kim CH, Co DT, Wasielewski MR, Schatz GC, Odom TW, Nat. Nanotechnol 2013, 8, 506. [PubMed: 23770807]

[7]. Berghuis AM, Serpenti V, Ramezani M, Wang S, Gómez Rivas J, J. Phys. Chem. C 2020, 124, 12030.

[8]. Heiderscheit TS, Oikawa S, Sanders S, Minamimoto H, Searles EK, Landes CF, Murakoshi K, Manjavacas A, Link S, J. Phys. Chem. Lett 2021, 12, 2516. [PubMed: 33667339]

[9]. Matricardi C, Hanske C, Garcia-Pomar JL, Langer J, Mihi A, Liz-Marzán LM, ACS Nano 2018, 12, 8531. [PubMed: 30106555]

[10]. Montjoy DG, Bahng JH, Eskafi A, Hou H, Kotov NA, J. Am. Chem. Soc 2018, 140, 7835. [PubMed: 29756778]

[11]. Palermo G, Rippa M, Conti Y, Vestri A, Castagna R, Fusco G, Suffredini E, Zhou J, Zyss J, De Luca A, Petti L, ACS Appl. Mater. Interfaces 2021, 13, 43715. [PubMed: 34469103]

[12]. Lenzi E, Jimenez de Aberasturi D, Liz-Marzán LM, ACS Sens. 2019, 4, 1126. [PubMed: 31046243]

[13]. Olson J, Manjavacas A, Basu T, Huang D, Schlather AE, Zheng B, Halas NJ, Nordlander P, Link S, ACS Nano 2016, 10, 1108. [PubMed: 26639191]

[14]. Yang F, Ye S, Dong W, Zheng D, Xia Y, Yi C, Tao J, Sun C, Zhang L, Wang L, Chen Q, Wang Y, Nie Z, Adv. Mater 2021, 33, 2100325.

[15]. Jeon J, Bhattarai K, Kim D-K, Kim JO, Urbas A, Lee SJ, Ku Z, Zhou J, Sci. Rep 2016, 6, 36190. [PubMed: 27805052]

[16]. Boles MA, Engel M, Talapin DV, Chem. Rev 2016, 116, 11220. [PubMed: 27552640]

[17]. Kasani S, Curtin K, Wu N, Nanophotonics 2019, 8, 2065.

[18]. Scarabelli L, Vila-Liarte D, Mihi A, Liz-Marzán LM, Acc. Mater. Res 2021, 2, 816.

[19]. Zhang H, Kinnear C, Mulvaney P, Adv. Mater 2020, 32, 1904551.

[20]. Mayer M, Tebbe M, Kuttner C, Schnepf MJ, König TAF, Fery A, Faraday Discuss. 2016, 191, 159. [PubMed: 27411967]

[21]. Rossner C, König TAF, Fery A, Adv. Opt. Mater 2021, 9, 2001869.

[22]. Molet P, Passarelli N, Pérez LA, Scarabelli L, Mihi A, Adv. Opt. Mater 2021, 9, 2100761.

[23]. Gupta V, Probst PT, Goßler FR, Steiner AM, Schubert J, Brasse Y, König TAF, Fery A, ACS Appl. Mater. Interfaces 2019, 11, 28189. [PubMed: 31298836]

[24]. Chiang N, Scarabelli L, Vinnacombe-Willson GA, Pérez LA, Dore C, Mihi A, Jonas SJ, Weiss PS, ACS Mater. Lett 2021, 3, 282. [PubMed: 34337418]

[25]. Dumond J, Low HY, Adv. Mater 2008, 20, 1291.

[26]. Perry JL, Herlihy KP, Napier ME, DeSimone JM, Acc. Chem. Res 2011, 44, 990. [PubMed: 21809808]

[27]. Lee T, Lee C, Oh DK, Badloe T, Ok JG, Rho J, Sensors 2020, 20, 4108.

[28]. Muench F, Schaefer S, Hagelüken L, Molina-Luna L, Duerrschnabel M, Kleebe H-J, Brötz J, Vaskevich A, Rubinstein I, Ensinger W, ACS Appl. Mater. Interfaces 2017, 9, 31142. [PubMed: 28825459]

[29]. Fortuni B, Inose T, Uezono S, Toyouchi S, Umemoto K, Sekine S, Fujita Y, Ricci M, Lu G, Masuhara A, Hutchison JA, Latterini L, Uji-i H, Chem. Commun 2017, 53, 11298.

[30]. Fortuni B, Fujita Y, Ricci M, Inose T, Aubert R, Lu G, Hutchison JA, Hofkens J, Latterini L, Uji-i H, Chem. Commun 2017, 53, 5121.

[31]. Zhang Q, Xu J-J, Liu Y, Chen H-Y, Lab. Chip 2008, 8, 352. [PubMed: 18231677]

[32]. Park K, Woo M-A, Lim J-A, Kim Y-R, Choi S-W, Lim M-C, Colloids Surf. Physicochem. Eng. Asp 2018, 558, 186.

[33]. Wang B, Chen K, Jiang S, Reincke F, Tong W, Wang D, Gao C, Biomacromolecules 2006, 7, 1203. [PubMed: 16602739]

[34]. Ellsworth AA, Walker AV, Langmuir 2016, 32, 2668. [PubMed: 26928276]

[35]. Lim M-C, Kim S-H, Park K, Kim Y-R, Kim J-H, Ok G, Choi S-W, RSC Adv. 2017, 7, 13228.

[36]. Stefik M, Guldin S, Vignolini S, Wiesner U, Steiner U, Chem. Soc. Rev 2015, 44, 5076. [PubMed: 25856171]

[37]. Lohmüller T, Aydin D, Schwieder M, Morhard C, Louban I, Pacholski C, Spatz JP, Biointerphases 2011, 6, MR1. [PubMed: 21428688]

[38]. Alvarez-Fernandez A, Cummins C, Saba M, Steiner U, Fleury G, Ponsinet V, Guldin S, Adv. Opt. Mater 2021, 9, 2100175.

[39]. Jeong H-H, Adams MC, Günther J-P, Alarcón-Correa M, Kim I, Choi E, Miksch C, Mark AF, Mark AG, Fischer P, ACS Nano 2019, 13, 11453. [PubMed: 31539228]

[40]. Huang L, Chen P-C, Liu M, Fu X, Gordiichuk P, Yu Y, Wolverton C, Kang Y, Mirkin CA, Proc. Natl. Acad. Sci 2018, 115, 3764. [PubMed: 29572429]

[41]. Cortés E, Camargo PH, Plasmonic Catalysis: From Fundamentals to Applications, John Wiley & Sons, 2021.

[42]. Ezendam S, Herran M, Nan L, Gruber C, Kang Y, Gröbmeyer F, Lin R, Gargiulo J, Sousa-Castillo A, Cortés E, ACS Energy Lett. 2022, 7, 778. [PubMed: 35178471]

[43]. Ao Z, Parasido E, Rawal S, Williams A, Schlegel R, Liu S, Albanese C, Cote RJ, Agarwal A, Datar RH, Lab. Chip 2015, 15, 4277. [PubMed: 26426331]

[44]. Lv S-W, Liu Y, Xie M, Wang J, Yan X-W, Li Z, Dong W-G, Huang W-H, ACS Nano 2016, 10, 6201. [PubMed: 27299807]

[45]. Park M-H, Reátegui E, Li W, Tessier SN, Wong KHK, Jensen AE, Thapar V, Ting D, Toner M, Stott SL, Hammond PT, J. Am. Chem. Soc 2017, 139, 2741. [PubMed: 28133963]

[46]. Vinnacombe-Willson GA, Chiang N, Scarabelli L, Hu Y, Heidenreich LK, Li X, Gong Y, Inouye DT, Fisher TS, Weiss PS, Jonas SJ, ACS Cent. Sci 2020, 6, 2105. [PubMed: 33274287]

[47]. Colburn M, Johnson SC, Stewart MD, Damle S, Bailey TC, Choi B, Wedlake M, Michaelson TB, Sreenivasan SV, Ekerdt JG, Willson CG, in (Ed.: Vladimirsky Y), Santa Clara, CA, 1999, p. 379.

[48]. Chou SY, Krauss PR, Renstrom PJ, J. Vac. Sci. Technol. B Microelectron. Nanometer Struct. Process. Meas. Phenom 1996, 14, 4129.

[49]. Espinha A, Dore C, Matricardi C, Alonso MI, Goñi AR, Mihi A, Nat. Photonics 2018, 12, 343. [PubMed: 29881447]

[50]. Dore C, Osmond J, Mihi A, Nanoscale 2018, 10, 17884. [PubMed: 30221647]

[51]. Merkel TJ, Herlihy KP, Nunes J, Orgel RM, Rolland JP, DeSimone JM, Langmuir 2010, 26, 13086. [PubMed: 20000620]

[52]. Tang J, Ou Q, Zhou H, Qi L, Man S, Nanomater. Basel Switz 2019, 9, 185.

[53]. Golze SD, Hughes RA, Rouvimov S, Neal RD, Demille TB, Neretina S, Nano Lett. 2019, 19, 5653. [PubMed: 31365267]

[54]. Demille TB, Hughes RA, Neretina S, J. Phys. Chem. C 2019, 123, 19879.

[55]. Kumar S, Yang H, Zou S, J. Phys. Chem. C 2007, 111, 12933.

[56]. Scarabelli L, Pure Appl. Chem 2018, 90, 1393.

[57]. Bastús NG, Comenge J, Puntes V, Langmuir 2011, 27, 11098. [PubMed: 21728302]

[58]. Landeke-Wilsmark B, Nyholm L, Hägglund C, Langmuir 2020, 36, 6848. [PubMed: 32531167]

[59]. Dunklin JR, Forcherio GT, Berry KR, Roper DK, J. Phys. Chem. C 2014, 118, 7523.

[60]. Campbell DJ, Villarreal RB, Fitzjarrald TJ, J. Chem. Educ 2012, 89, 1312.

[61]. Scarabelli L, Sánchez-Iglesias A, Pérez-Juste J, Liz-Marzán LM, J. Phys. Chem. Lett 2015, 6, 4270. [PubMed: 26538043]

[62]. Liz-Marzán LM, Kagan CR, Millstone JE, ACS Nano 2020, 14, 6359. [PubMed: 32575172]

[63]. Demille TB, Hughes RA, Dominique N, Olson JE, Rouvimov S, Camden JP, Neretina S, Nanoscale 2020, 12, 16489. [PubMed: 32790810]

[64]. Liu G, Zhang C, Wu J, Mirkin CA, ACS Nano 2015, 9, 12137. [PubMed: 26562365]

[65]. Ashley MJ, Bourgeois MR, Murthy RR, Laramy CR, Ross MB, Naik RR, Schatz GC, Mirkin CA, J. Phys. Chem. C 2018, 122, 2307.

[66]. Kuttner C, Piotto V, Liz-Marzán LM, Chem. Mater 2021, 33, 8904.

[67]. Hanske C, González-Rubio G, Hamon C, Formentín P, Modin E, Chuvilin A, Guerrero-Martínez A, Marsal LF, Liz-Marzán LM, J. Phys. Chem. C 2017, 121, 10899.

[68]. Chhour P, Kim J, Benardo B, Tovar A, Mian S, Litt HI, Ferrari VA, Cormode DP, Bioconjug. Chem 2017, 28, 260. [PubMed: 28095688]

[69]. Sun Y, Chem. Mater 2007, 19, 5845.

[70]. Lohmueller T, Bock E, Spatz JP, Adv. Mater 2008, 20, 2297.

[71]. Brown KR, Walter DG, Natan MJ, Chem. Mater 2000, 12, 306.

[72]. Pastoriza-Santos I, Liz-Marzán LM, Langmuir 2002, 18, 2888.

[73]. Tao AR, Habas S, Yang P, Small 2008, 4, 310.

[74]. Shi Q, Gómez DE, Dong D, Sikdar D, Fu R, Liu Y, Zhao Y, Smilgies D-M, Cheng W, Adv. Mater 2019, 31, 1900989.

[75]. Cheng Q, Song L, Lin H, Yang Y, Huang Y, Su F, Chen T, Langmuir 2020, 36, 250. [PubMed: 31697894]

[76]. Jimenez de Aberasturi D, Serrano-Montes AB, Langer J, Henriksen-Lacey M, Parak WJ, Liz-Marzán LM, Chem. Mater 2016, 28, 6779.

[77]. Giner-Casares JJ, Henriksen-Lacey M, García I, Liz-Marzán LM, Angew. Chem. Int. Ed 2016, 55, 974.

[78]. Lenzi E, Jimenez de Aberasturi D, Henriksen-Lacey M, Piñeiro P, Muniz AJ, Lahann J, Liz-Marzán LM, ACS Appl. Mater. Interfaces 2022, 14, 20708. [PubMed: 35487502]

[79]. Casu A, Cabrini E, Donà A, Falqui A, Diaz-Fernandez Y, Milanese C, Taglietti A, Pallavicini P, Chem. - Eur. J 2012, 18, 9381. [PubMed: 22736477]

[80]. Kim J-Y, Yeom J, Zhao G, Calcaterra H, Munn J, Zhang P, Kotov N, J. Am. Chem. Soc 2019, 141, 11739. [PubMed: 31329438]

[81]. Goerlitzer ESA, Mohammadi R, Nechayev S, Volk K, Rey M, Banzer P, Karg M, Vogel N, Adv. Mater 2020, 32, 2001330.

[82]. Probst PT, Mayer M, Gupta V, Steiner AM, Zhou Z, Auernhammer GK, König TAF, Fery A, Nat. Mater 2021, 20, 1024. [PubMed: 33927391]

[83]. Juodėnas M, Tamulevičius T, Henzie J, Erts D, Tamulevičius S, ACS Nano 2019, 13, 9038. [PubMed: 31329417]

[84]. Manjavacas A, Zundel L, Sanders S, ACS Nano 2019, 13, 10682. [PubMed: 31487460]

[85]. Le-Van Q, Zoethout E, Geluk E-J, Ramezani M, Berghuis M, Gómez Rivas J, Adv. Opt. Mater 2019, 7, 1801451.

[86]. Volk K, Honold T, Feller D, Karg M, Adv. Mater. Interfaces 2021, 8, 2100317.

[87]. Brasse Y, Gupta V, Schollbach HCT, Karg M, König TAF, Fery A, Adv. Mater. Interfaces 2020, 7, 1901678.

[88]. Osinkina L, Lohmüller T, Jäckel F, Feldmann J, J. Phys. Chem. C 2013, 117, 22198.

[89]. Mark AG, Gibbs JG, Lee T-C, Fischer P, Nat. Mater 2013, 12, 802. [PubMed: 23793159]

[90]. Klös G, Miola M, Sutherland DS, J. Phys. Chem. C 2019, 123, 7347.

[91]. Klös G, Andersen A, Miola M, Birkedal H, Sutherland DS, Nano Res. 2019, 12, 1635.

[92]. Viswanath B, Kundu P, Halder A, Ravishankar N, J. Phys. Chem. C 2009, 113, 16866.

[93]. Shi Y, Lyu Z, Zhao M, Chen R, Nguyen QN, Xia Y, Chem. Rev 2021, 121, 649. [PubMed: 32667792]

[94]. Abdel-Halim ES, Al-Deyab SS, Carbohydr. Polym 2011, 86, 1615.

[95]. Wu X, Lu C, Zhou Z, Yuan G, Xiong R, Zhang X, Environ. Sci. Nano 2014, 1, 71.

[96]. Liu Y-C, Chuang TC, J. Phys. Chem. B 2003, 107, 12383.

[97]. Han J, Li L, Guo R, Macromolecules 2010, 43, 10636.

[98]. Wang C, Flynn NT, Langer R, Adv. Mater 2004, 16, 1074.

[99]. Li J, Xie J, Gao L, Li CM, ACS Appl. Mater. Interfaces 2015, 7, 2726. [PubMed: 25580718]

[100]. Song B, He K, Yuan Y, Sharifi-Asl S, Cheng M, Lu J, Saidi WA, Shahbazian-Yassar R, Nanoscale 2018, 10, 15809. [PubMed: 30102314]

[101]. Jain T, Lara-Avila S, Kervennic Y-V, Moth-Poulsen K, Nørgaard K, Kubatkin S, Bjørnholm T, ACS Nano 2012, 6, 3861. [PubMed: 22494354]

[102]. Mieszawska AJ, Slawinski GW, Zamborini FP, J. Am. Chem. Soc 2006, 128, 5622. [PubMed: 16637614]

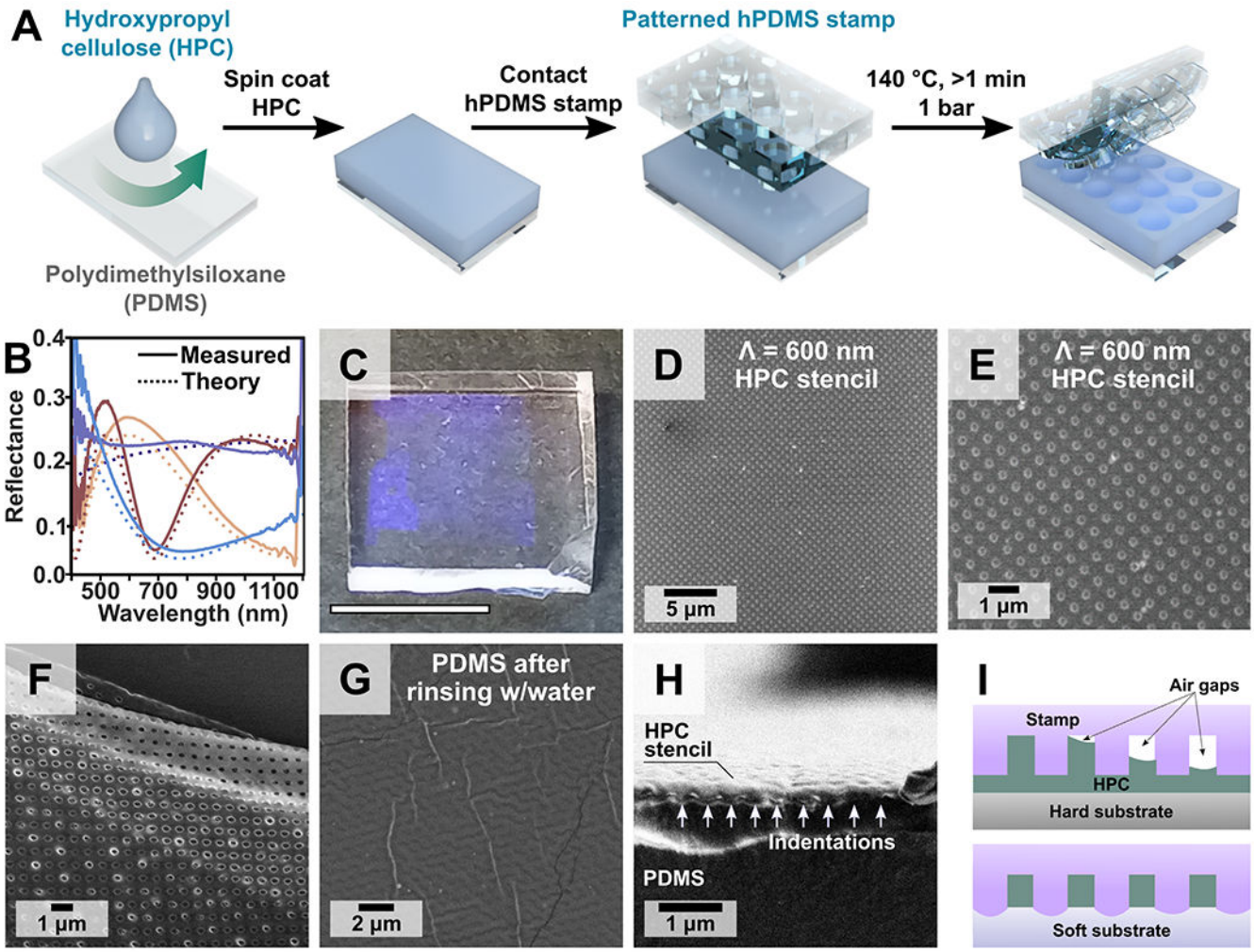

Figure 1.

A: Schematic of hydroxypropyl cellulose (HPC) thermal nanoimprint lithography on polydimethylsiloxane (PDMS). **B:** Reflectance spectra giving the estimated thickness of the films on silicon: 30 nm (solid purple), 125 nm (solid blue), 192 nm (solid orange), and 330 nm (solid red) for the HPC aqueous solutions at different concentrations. The dotted lines are the corresponding simulated interference generated by differential refraction for thin films with heights of 30 nm (dotted purple), 125 nm (dotted blue), 192 nm (dotted orange), and 330 nm (dotted red). **C:** Photograph of the ~30 nm patterned HPC stencil with periodicities of 600 nm (Λ) resulting from the 21 mg/mL aqueous HPC solution (patterned area is 0.49 cm^2, scale bar: 0.7 cm). **D-F:** Scanning electron micrographs of different areas of the thinnest (30 nm) patterned HPC layer, with **F** showing a region at the edge of the film where holes are clearly visible. **G**: the PDMS substrate after removal of the HPC with water (indentation can be clearly observed), and **H:** the cross-section of a PDMS substrate with the imprinted HPC. **I:** Schematic showing imprinting of an HPC film with volume lower than the negative volume of the stamp on a hard (*top*) and soft (*bottom*) substrate. Details of sample preparation can be found in the Supporting Information, Scheme S3.

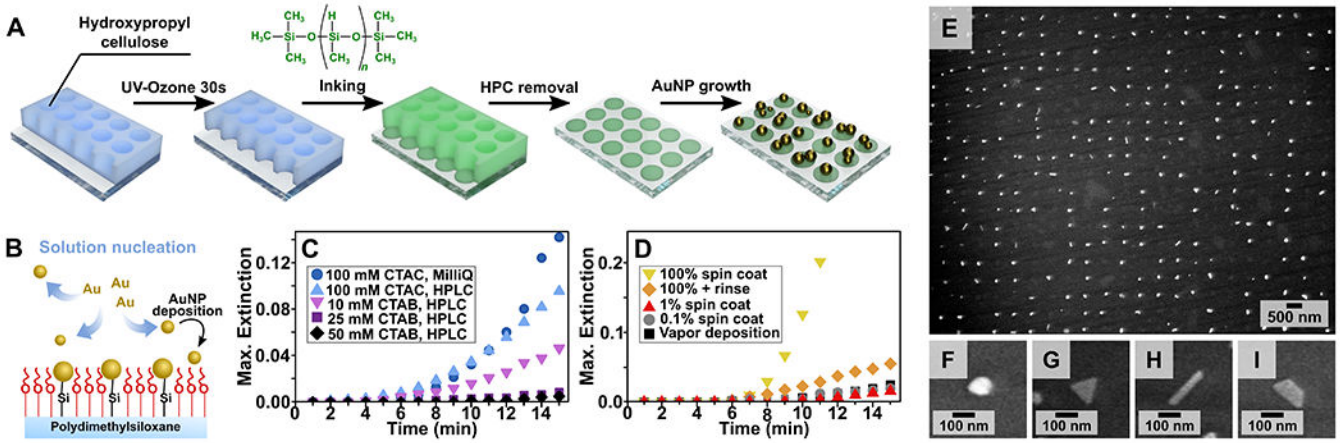

Figure 2.

A: Schematic of the etching of the residual layer with UV-ozone, followed by inking with polymethylhydrosiloxane, removal of the hydroxypropyl cellulose (HPC) with water, and introduction of the substrate into a growth solution to form gold nanoparticles (AuNPs). **B:** Scanning electron micrograph obtained under environmental conditions (60 Pa, air) showing the patterned array after 10 min growth. **C**: Schematic depicting competition between secondary solution nucleation and surface growth. **D:** Maximum extinction of growth solutions containing different water sources (Milli-Q or high-performance liquid chromatography, HPLC, water) and surfactant/capping ligand conditions (cetyltrimethylammonium bromide or chloride, CTAB/C, respectively), and all applying ascorbic acid as a mild reductant, over 15 min. **E:** Maximum extinction of growth solutions for substrates with different inking conditions. **F-I:** Scanning electron microscopy images showing a mixture of products suggesting different crystal structures and twinning: (**F**) isotropic products, (**G**) triangles, (**H**) rods, and (**I**) platelets/truncated triangles.

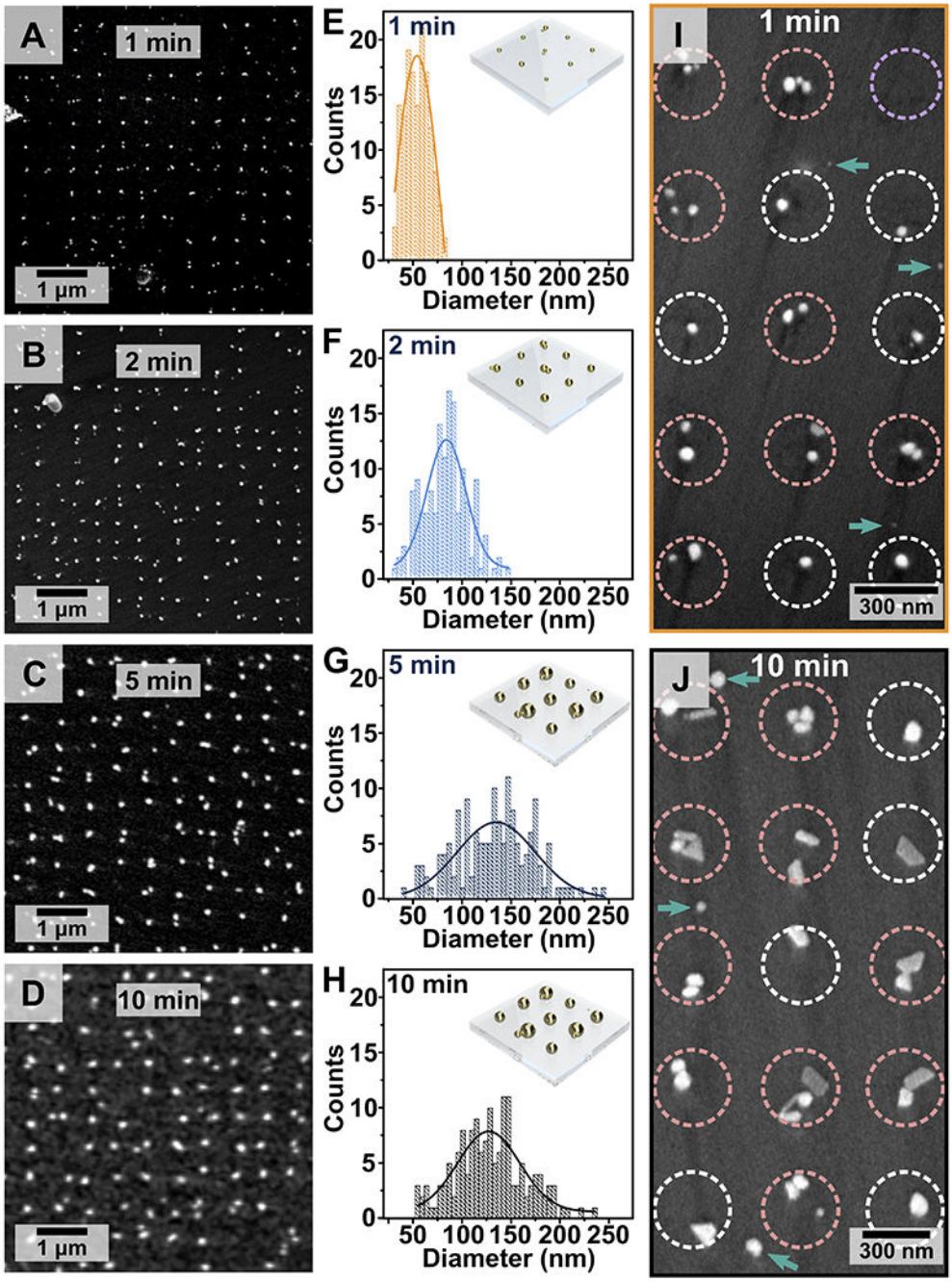

Figure 3.

A-D: Scanning electron microscopy (SEM) images of patterned nanoparticle substrates after (**A**) 1 min, (**B**) 2 min, (**C**) 5 min, and (**D**) 10 min growth with a growth solution containing cetyltrimethylammonium bromide (capping ligand/surfactant), gold salt, and ascorbic acid as a mild reducing agent. **E-H:** Size distributions for the (**E**) 1 min, (**F**) 2 min, (**G**) 5 min, and (**H**) 10 min samples (150 nanoparticles each, n=10). **I,J:** Representative SEM images showing pattern yield and common defects: multiple particles per area (*pink circles*),

vacancies (*purple circles*) and particles outside the pattern (*green arrows*). Patterned regions with single particles are indicated with a white circle (n=10).

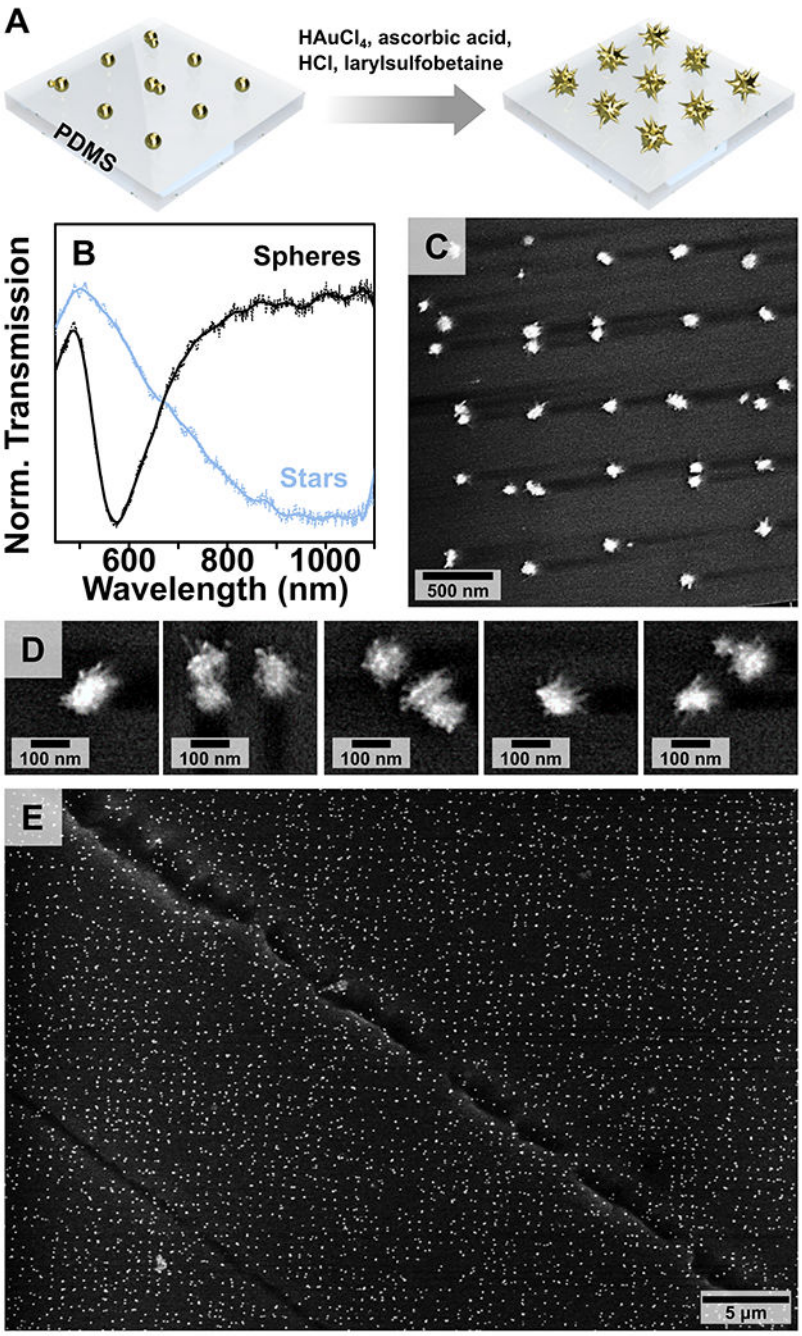

Figure 4.

A: Schematic of overgrowth process into nanostars on polydimethylsiloxane (PDMS). **B:** Normalized and smoothed (Savitzky-Golay) transmission spectra comparing the plasmon band position before (5 min growth in cetyltrimethylammonium bromide solution with ascorbic acid added as a weak reducing agent) and after stars overgrowth (5 min in a solution containing capping ligand/surfactant laurylsulfobetaine, HCl and ascorbic acid). **C-E:** Scanning electron microscopy images of the nanostar arrays at different magnifications.

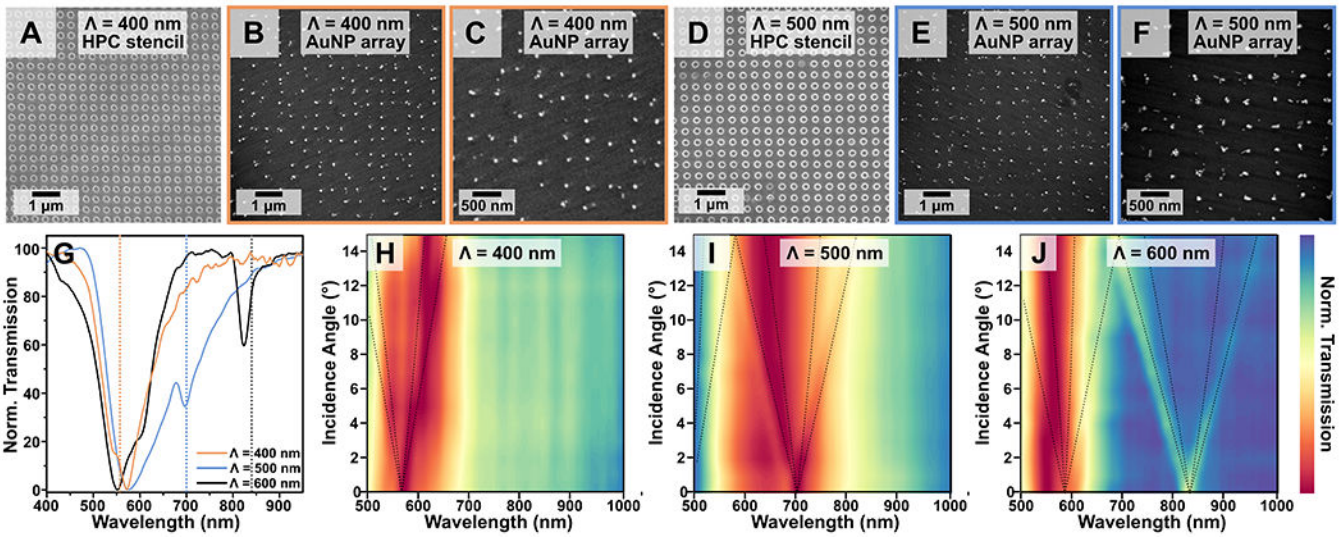

Figure 5.

Scanning electron microscope (SEM) images showing **A:** patterned hydroxypropyl cellulose (HPC) films with lattice parameter Λ = 400 nm and **B,C:** the resulting patterned nanoparticle substrates. SEM images showing the **D:** an Λ = 500 nm stencil and **E,F:** the corresponding patterned nanoparticles (SEM data for the Λ = 600 nm HPC stencils and resulting gold nanoparticle arrays are shown in Figures 1, 3). **G:** Smoothed (Savitzky-Golay) and normalized transmission spectra of the substrates following refractive index matching. Dashed lines represent the theoretical position of Rayleigh-Wood anomalies (n_{PDMS}=1.4). **H-J:** Contour plots showing measured angular dependence of the optical response optima for the (**H**) Λ = 400 nm, (**I**) Λ = 500 nm, and (**J**) Λ = 600 nm lattices. Dashed lines represent the predicted positions of the Rayleigh anomalies using n_{PDMS} = 1.4. Additional SEM images can be found in the Supporting Information, Figures S13–S15. All arrays were fabricated after 5 min of growth in the cetyltrimethylammonium bromide/ascorbic acid solution optimized from Figure 2 to limit secondary nucleation.